

Label-free Detection of Lymph Node Metastases with US-guided Functional Photoacoustic Imaging¹

Geoffrey P. Luke, PhD
Stanislav Y. Emelianov, PhD

Purpose:

To determine the ability of ultrasonography (US)-guided spectroscopic photoacoustic (sPA) imaging to depict changes in blood oxygen saturation (SO₂) in metastatic lymph nodes of a mouse model of oral cancer.

Materials and Methods:

All studies were performed by following protocols approved by the institutional animal care and use committee at the University of Texas at Austin. Coregistered US and photoacoustic images were acquired spanning volumes containing a total of 31 lymph nodes in 17 female *nu/nu* mice. The mice were either healthy (three mice, five nodes) or bearing a primary tumor consisting of luciferase-labeled FaDu cells (14 mice, 26 nodes). Ten photoacoustic images acquired with optical wavelengths spanning from 680 to 860 nm were spectrally unmixed by using a linear least-squares method to obtain sPA images. After imaging, histologic analysis enabled confirmation of the presence of micrometastases. Generalized estimating equations were used to compare metastatic and normal lymph nodes, with a *P* value of .05 taken to indicate a significant difference. Sensitivity and specificity were determined with a receiver operator characteristic curve constructed from the background-subtracted SO₂ values.

Results:

Metastatic lymph nodes (*n* = 7) exhibited a significantly (*P* = .018) lower spatially averaged background-subtracted SO₂ (mean, 5.4% ± 3.5 [standard error]) when compared with lymph nodes without metastases (mean, 13.7% ± 1.3; *n* = 24). This effect was observed throughout the entire volume of the nodes rather than being limited to the metastatic foci. The change in SO₂, which was inversely related to the size of the metastasis, was detectable in metastases as small as 2.6 × 10⁻³ mm³.

Conclusion:

The results show that US-guided sPA imaging is capable of depicting changes in SO₂ in lymph nodes that were correlated with metastatic invasion.

©RSNA, 2015

¹From the Department of Biomedical Engineering, the University of Texas at Austin, 107 W Dean Keeton St, Austin, TX 78712; and Department of Imaging Physics, the University of Texas MD Anderson Cancer Center, Houston, Tex. Received August 11, 2014; revision requested October 2; revision received February 16, 2015; accepted March 16; final version accepted March 24. Supported by Department of Defense grant W81XWH-14-1-0356 and the Breast Cancer Research Foundation. Address correspondence to S.Y.E. (e-mail: emelian@mail.utexas.edu).

Over 90% of cancer-related deaths can be attributed either directly or indirectly to the metastatic spread of disease (1). Thus, determining the spread of cancer from a primary tumor is of paramount importance in cancer staging and in the development of a treatment strategy. In many types of cancer, including skin, head and neck, breast, and gastrointestinal cancers, the presence of malignant cells in the first lymph node to which a tumor drains—known as the sentinel lymph node (SLN)—is a harbinger of distant metastases and a low survival rate. SLN biopsies guided by peritumoral injection of dye, a radioactive colloid, or both have gained widespread acceptance in cancer staging (2–4). However, these biopsies are invasive procedures that expose the patient to radioactive compounds, have a high level of morbidity, and may require 2 or more weeks to obtain results (5,6).

A number of efforts have been made to improve or replace the SLN biopsy procedure with biomedical imaging (7,8). For example, positron emission tomography (PET) with fludeoxyglucose administration has shown an ability to depict metastases as small as 80 mm³ in the lymphatic system of patients with melanoma (9). Although PET has excellent sensitivity, it requires the use of ionizing radiation and has relatively poor resolution. Recently, optical imaging has been proposed as a tool with which to not only map the SLN but also detect molecular signatures of metastases (10,11). Optical imaging, however, has limited sensitivity at depth, and its resolution quickly degrades at depths of more than 1 mm (12). Ultrasonography (US) provides a desirable alternative because it is nonionizing, it can provide high-resolution images

at depths of several centimeters, and it is capable of real-time imaging. US imaging can depict anatomic and functional changes in the lymphatic system that are associated with the invasion of metastatic cells (7,8,13–15). Although US imaging can reliably depict a large proportion of metastatic lymph nodes, it has not yet shown the sensitivity and specificity required to replace SLN biopsy in the staging of cancer.

Recently, photoacoustic (PA) imaging has been proposed as a tool to aid in the evaluation of lymph node metastasis. PA imaging is an emerging hybrid imaging technique that relies on the detection of acoustic waves that are generated by the thermoelastic expansion of tissue after it is irradiated with a pulsed laser (16–19). It combines the high resolution of US with excellent optical contrast. By administering optically absorbing contrast agents, SLN mapping has been demonstrated in small-animal models (20–23). Furthermore, by targeting plasmonic nanoparticles to cell surface receptors associated with the primary tumor, sensitive detection of micrometastases can be achieved (24). However, these promising techniques have yet to have a clinical effect. This is largely due to the fact that they do not directly indicate the metastatic state of the SLN or that they require the use of metal nanoparticles, which have yet to gain clinical acceptance. One advantage of photoacoustic imaging is that the blood oxygen saturation (SO₂) can

be noninvasively measured without the need for exogenous contrast agents (25). Thus far, this technique has been primarily restricted to the analysis of hypoxia in primary tumors (17).

The purpose of this study was to determine the ability of US-guided spectroscopic PA (sPA) imaging to detect changes in SO₂ in metastatic lymph nodes of a mouse model of oral cancer.

Materials and Methods

Animal Studies

All studies were performed after protocols were approved by the institutional animal care and use committee at the University of Texas at Austin. A metastatic orthotopic mouse model of squamous cell carcinoma in the oral cavity was selected for this study (26). A priori power analysis (G*Power Software; Heinrich-Heine-Universität Düsseldorf, Düsseldorf, Germany) indicated that five lymph nodes per group were needed to achieve the power threshold of 0.8. The primary tumor was initiated with submucosal inoculation of approximately 300 000 FaDu cells (ATCC, Manassas, Va) labeled with a

Published online before print

10.1148/radiol.2015141909 Content codes:  

Radiology 2015; 000:1–8

Abbreviations:

PA = photoacoustic
SLN = sentinel lymph node
SO₂ = oxygen saturation
sPA = spectroscopic PA

Author contributions:

Guarantors of integrity of entire study, G.P.L., S.Y.E.; study concepts/study design or data acquisition or data analysis/interpretation, G.P.L., S.Y.E.; manuscript drafting or manuscript revision for important intellectual content, G.P.L., S.Y.E.; approval of final version of submitted manuscript, G.P.L., S.Y.E.; agrees to ensure any questions related to the work are appropriately resolved, G.P.L., S.Y.E.; literature research, G.P.L., S.Y.E.; experimental studies, G.P.L., S.Y.E.; statistical analysis, G.P.L., S.Y.E.; and manuscript editing, G.P.L., S.Y.E.

Funding:

This research was supported by the National Institutes of Health (grants R01EB008101 and F31CA168168).

Conflicts of interest are listed at the end of this article.

Implications for Patient Care

- In patients with a diagnosis of primary tumor, US examination of lymph nodes combined with sPA imaging may result in a sensitive noninvasive clinical tool capable of depicting small metastases.
- By using US-guided photoacoustic imaging, which is a noninvasive technique, the need for sentinel lymph node biopsy potentially could be reduced and ultimately eliminated, resulting in fewer incidents of patient morbidity.

Advance in Knowledge

- Label-free spectroscopic photoacoustic (sPA) imaging can depict decreased blood oxygen saturation in the metastatic cervical lymph nodes of tumor-bearing mice.

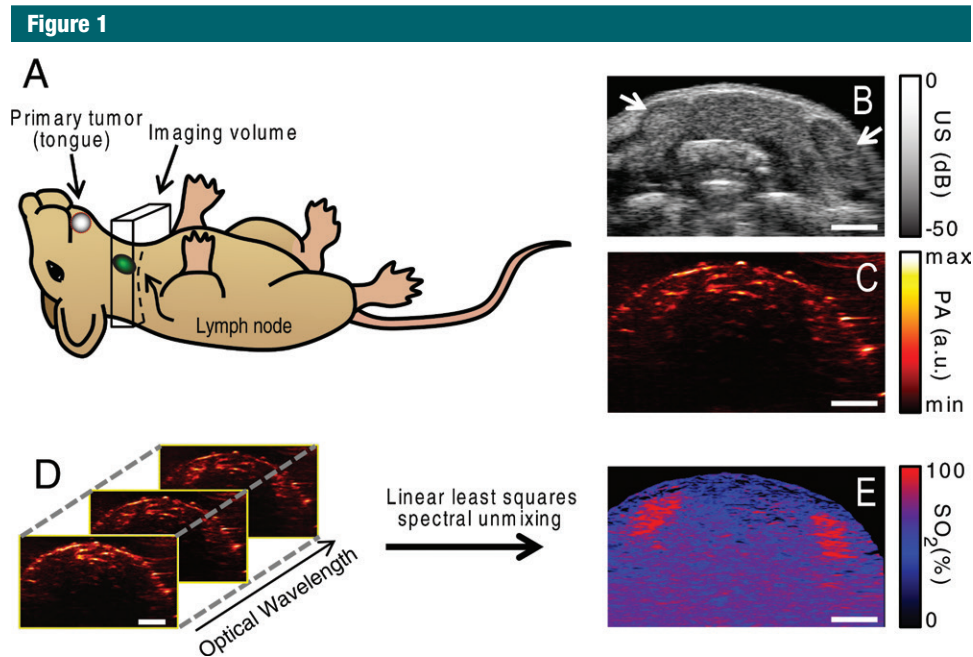


Figure 1: A, Schematic drawing depicts the location of the primary tumor, cervical lymph nodes, and imaging volume used in this study. B, Representative two-dimensional US image shows the cervical lymph nodes (arrows). C, Coregistered PA image. D, Ten single-wavelength PA images were acquired in each imaging plane. E, A linear least-squares spectral unmixing algorithm was used to calculate the sPA image depicting the SO₂. Scale bars are 2 mm.

luciferase reporter in the tongues of 18 female *nu/nu* nude mice (Charles River Laboratories, Boston, Mass). After 2–3 weeks, a primary tumor with a diameter of 3–4 mm had formed in 14 mice. Mice that did not develop a primary tumor were excluded from this study. Prior to undergoing US and PA imaging, the mice were anesthetized with a combination of isoflurane (1.5%–2.0%) and O₂ (0.5 L/min). Respiration rate, heart rate, and body temperature were monitored with a heated electrocardiogram pad (Visualsonics, Toronto, Ontario, Canada).

After the imaging studies, mice were euthanized with an overdose of isoflurane (5%) and cervical dislocation. The cervical lymph nodes were excised and fixed in 10% formalin for 24–48 hours and were transferred to 70% ethanol. The fixed lymph nodes were embedded in paraffin and sliced in levels of 100 μ m. A slice from each level was stained with hematoxylin-eosin to visualize cell morphology

and identify micrometastases. Finally, manual tracing with ImageJ software (National Institutes of Health, Bethesda, Md) was used to measure the cross-sectional area of each slice of all metastases in the lymph nodes. The volume of each metastasis was estimated by summing the product of cross-sectional area and the level thickness (100 μ m) from each slide containing part of the metastasis.

PA and US Imaging

Imaging was performed by using a Vevo LAZR small-animal US and PA imaging system (Visualsonics). An LZ-550 linear-array transducer (256 elements, 40-MHz center frequency, 27-MHz bandwidth) was used to acquire all PA and US images. The tunable laser of this system supplied 10–20 mJ per pulse across its 680–970-nm wavelength range, with a pulse repetition frequency of 10 Hz. The B-mode US images were constructed from 128 focused transmit lines, with one focal

zone corresponding to the depth of the lymph nodes. All imaging examinations were performed in a 5 \times 14 \times 15 mm volume containing the cervical lymph nodes, which were the site of metastasis in this mouse model (Fig 1, A). The primary tumor was not imaged. Two-dimensional coregistered US (Fig 1, B) and PA (Fig 1, C) images were acquired as the transducer was scanned in the out-of-plane direction with a linear motor. The lymph nodes were identified as hypoechoic bean-shaped regions on the US images (Fig 1, B), and manual segmentation of the images was used for statistical analysis. In each plane, photoacoustic images with excitation optical wavelengths of 680, 700, 720, 740, 760, 780, 800, 820, 840, and 860 nm were acquired to construct the sPA images (Fig 1, D). Each image was normalized with the measured laser energy to account for pulse-to-pulse and wavelength-dependent fluctuations in energy. Further processing of the images was

performed offline with Matlab software (Mathworks, Natick, Mass).

Spectroscopic Processing

A linear least-squares spectral unmixing algorithm (27) was used to identify the relative contributions of the predominant endogenous absorbers in the lymph nodes (ie, deoxyhemoglobin [Hb] and oxyhemoglobin [Hb_{o2}]) to the overall PA signal (Fig 1, E). The PA signal, P , generated by an N distinct absorbers immediately after a laser pulse with wavelength λ can be written as follows:

$$P(\lambda) = \Gamma F(\lambda) [C(1) \varepsilon_1(\lambda) + C(2) \varepsilon_2(\lambda) + \dots + C(N) \varepsilon_N(\lambda)], \quad (1)$$

where Γ is the Grüneisen parameter, F is the laser fluence, $C[i]$ is the concentration of the i^{th} absorber, and ε_i is the molar absorption coefficient for the i^{th} absorber. In this study, we restricted our spectral analysis to Hb and Hb_{o2}. The absorption spectrum for Hb and Hb_{o2} was obtained from the literature (28). By varying λ and acquiring multiple PA images, Equation 1 becomes a set of independent linear equations. After estimating F and Γ , the relative concentrations of Hb and Hb_{o2} ($C[\text{Hb}]$ and $C[\text{Hb}_{o2}]$, respectively) were estimated for each pixel in a minimum mean squared error sense by calculating the pseudoinverse of a matrix containing the absorption spectra of the photoabsorbers, ε^* :

$$C = \varepsilon^* \left(\frac{P}{\Gamma F} \right) \quad (2)$$

The SO₂ was then calculated in each pixel, as follows:

$$SO_2 = \frac{C[\text{Hb}_{o2}]}{C[\text{Hb}_{o2}] + C[\text{Hb}]} \quad (3)$$

Statistical Analysis

The true metastatic state of the lymph nodes was determined at histologic analysis of samples stained with hematoxylin-eosin. Lymph nodes with metastases nearby (eg, in the afferent lymphatic vessels) but not within their

boundaries were taken to be healthy (seven nodes). For each lymph node, SO₂ throughout the entire lymph node volume (as segmented from the US images) was averaged. The SO₂ from the 2-mm-thick layer of tissue immediately surrounding each lymph node was also calculated to account for mouse-to-mouse variations in background SO₂. This background SO₂ was subtracted from the nodal SO₂ for all further analysis. Generalized estimating equations (geepack for R software; R Foundation for Statistical Computing, Vienna, Austria) (29) were used to determine if background-subtracted SO₂ in metastatic nodes was significantly lower than that in healthy nodes. A P value of less than .05 indicated a significant difference. Measured SO₂ values are represented as the average \pm standard error, with 95% confidence intervals in parentheses.

The relationship between metastasis volume (as measured at histologic examination) and SO₂ was determined with linear regression analysis by using the Curve Fitting Toolbox in Matlab (Mathworks). The resulting R^2 value was used to evaluate the strength of this relationship. A receiver operator characteristic curve was constructed by sorting all lymph nodes by their mean background-subtracted SO₂. The true-positive and false-positive rates were calculated by increasing the SO₂ used for classification in a stepwise fashion, with histologic results indicating ground truth.

Results

Representative US, PA, and histologic images are shown in Figure 2. Healthy and metastatic cervical lymph nodes are easily identifiable on US images as hypochoic bean-shaped regions (Fig 2). The sPA images (Fig 2, F–J) show that the lymph nodes have a higher oxygenation level than does the surrounding glandular tissue. This is likely due to the fact that the lymph nodes are well-perfused organs. The sPA images show qualitatively that SO₂ in the lymph nodes varies with the extent of metastatic involvement. Healthy lymph nodes (Fig 2, A, F, K), lymph nodes

with metastases nearby (Fig 2, B, G, L), and lymph nodes harboring small (<100 μm) metastases (Fig 2, C, H, M) all have similar levels of SO₂. Those lymph nodes with a higher metastatic burden show decreased SO₂ throughout their volume (Fig 2, D, I, N, E, J, O). The effect is seen when metastases are as small as $2.6 \times 10^{-3} \text{ mm}^3$, which represents only 1% of the entire nodal volume.

By using the photoacoustic measurements of blood SO₂ averaged throughout the entire volume of the lymph nodes, a clear difference is seen between healthy and metastatic lymph nodes (Fig 3). The average background-subtracted SO₂ in metastatic nodes ($5.4\% \pm 3.5$; 95% confidence interval: $-1.5, 12.2$; $n = 7$) was significantly ($P = .018$) lower than that in healthy nodes ($13.7\% \pm 1.3$; 95% confidence interval: $11.3\%, 16.2\%$; $n = 24$). No statistical difference ($P = .89$) was observed between two subgroups of healthy nodes: those with metastases nearby (background-subtracted SO₂, $14.1\% \pm 2.7$; 95% confidence interval: $8.8\%, 19.4\%$; $n = 7$) and those without metastases in the region (background-subtracted SO₂, $13.6\% \pm 2.8$; 95% confidence interval: $10.8\%, 16.4\%$; $n = 14$). This suggests that the functional changes resulting in decreased SO₂ occur only once the tumor has invaded the lymph node; metastases in the lymphatic vessels do not trigger this effect.

We found that the average SO₂ in lymph nodes was inversely related ($R^2 = 0.80$) to the volume of the metastasis, although this relationship is primarily driven by the largest metastasis (Fig 4). Overall, the background-subtracted SO₂ proved to be a moderate predictor of the metastatic state of the lymph nodes in this study. The receiver operator characteristic curve (Fig 5) shows that sensitivity and specificity of 71% and 83%, respectively, were achieved (Table). The area under the receiver operating characteristic curve was 0.79.

Discussion

The ability to noninvasively detect metastases in the lymphatic system at a

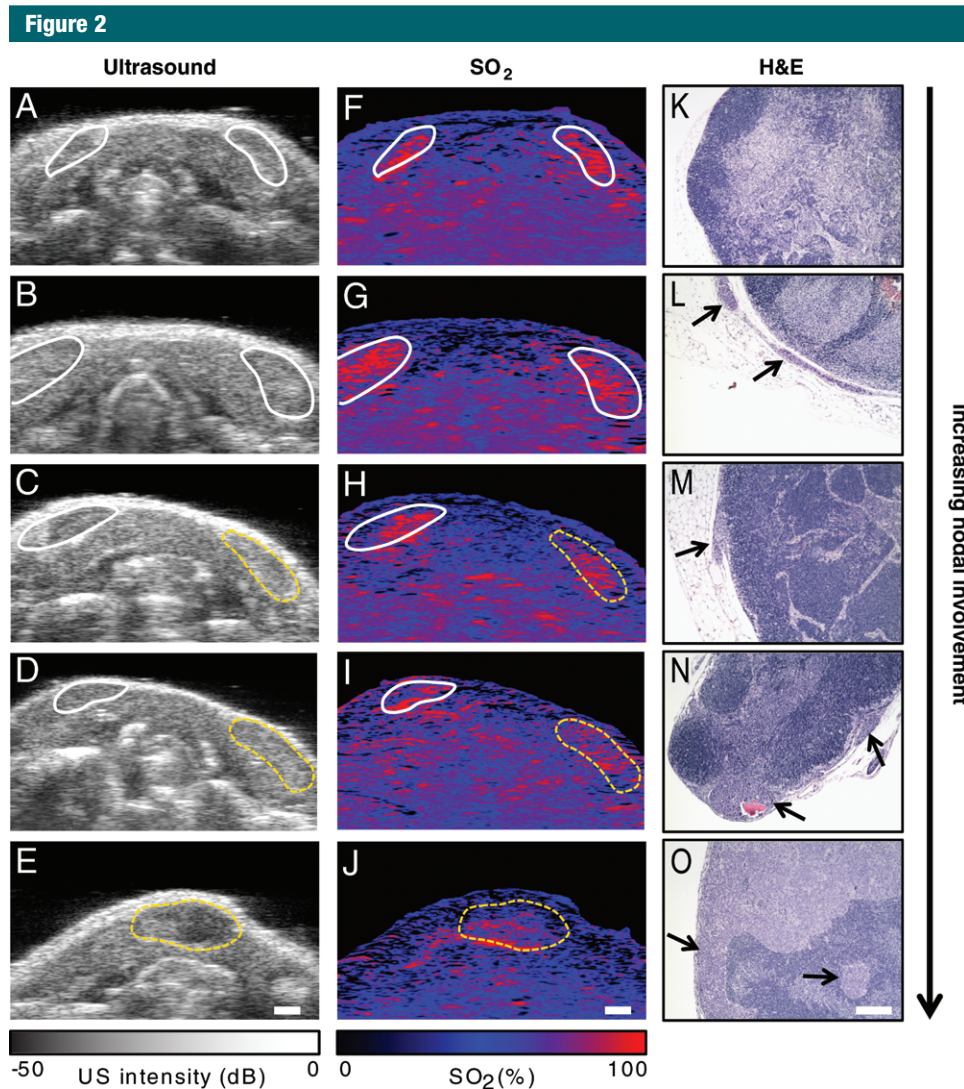


Figure 2: Representative, *A–E*, US, *F–J*, sPA, and *K–O*, hematoxylin-eosin–stained histologic images of tissue from a mouse without metastases *A, F, K*, Images in a mouse with metastasis in a nearby lymphatic vessel. *B, G, L*, Images in a mouse with a 50-µm metastasis at the edge of the node, *C–E, H–J, M–O*, Images in mice with higher metastatic burdens. Normal lymph nodes are denoted by solid white outlines on US and sPA images, while metastatic nodes are denoted by dashed yellow outlines. Micrometastases are indicated by arrows in the hematoxylin-eosin–stained images. Scale bars are 1 mm (*A–J*) or 100 µm (*K–O*).

microscale could prove to be valuable in the diagnosis and staging of cancer, with the potential to decrease the morbidity associated with sentinel lymph node biopsies. The results shown here indicate that the widespread decreased nodal SO_2 associated with the early stages of metastatic invasion could yield a way to drastically improve the sensitivity of current methods. Because the metastases are still small, they likely

have not progressed to a point where hypoxic conditions could arise (30). Thus, the change in SO_2 is likely to be driven by other processes in the lymphatic system. It is possible that these functional changes are due to increased metabolic activity of normal cells (eg, macrophages) in the region that are responding to the metastatic invasion. It is expected that continued tumor progression will lead to a larger decrease

in SO_2 , as tumor hypoxia contributes to the effect. Indeed, it has been shown that hypoxia in SLN metastases in patients with breast cancer is correlated with hypoxia in the primary tumor (31).

In contrast to most other proposed imaging methods with which to detect SLN metastasis (9,11,32), sPA imaging of nodal SO_2 requires no exogenous contrast agents. The contrast is driven by functional changes within the node,

Figure 3

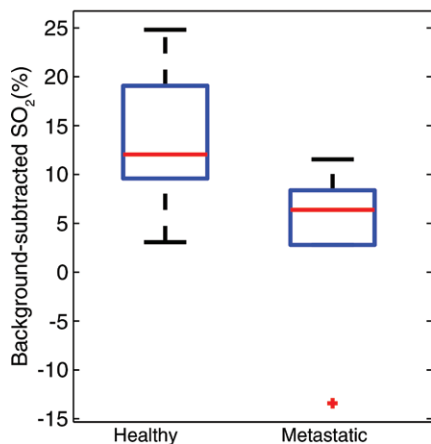


Figure 3: Box-and-whisker plot indicates healthy lymph nodes ($n = 24$) exhibited a significantly higher average SO_2 than did metastatic nodes ($n = 7$, $P = .018$).

Figure 4

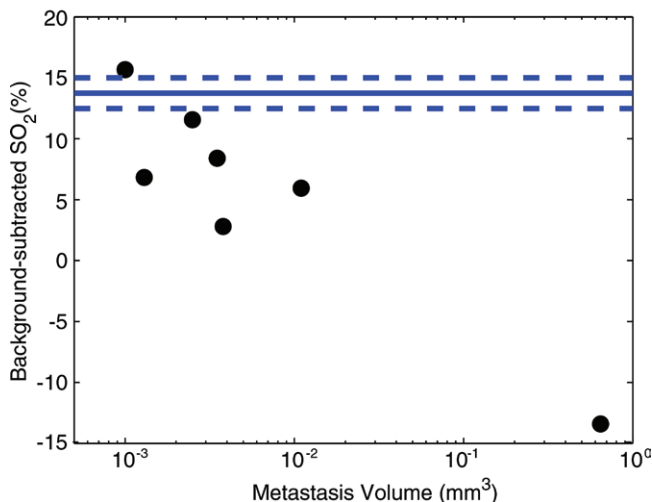


Figure 4: Scatterplot shows that average SO_2 is inversely related ($R^2 = 0.80$) to the volume of the metastasis in the lymph node, as measured at histologic analysis. The solid blue line indicates average SO_2 in healthy nodes, while the dashed blue lines indicates standard error.

rather than by molecular expressions. Alternative approaches to measure tissue oxygenation require either excising the tissue and performing immunohistochemistry or using an invasive oxygen probe to measure a single point. In addition, PET imaging of hypoxic-sensitive agents (eg, fluorine 18 fluoromisonidazole) can be used to visualize hypoxia in tumors (33). Spectroscopic photoacoustic imaging, conversely, can be used to noninvasively measure the SO_2 of hemoglobin with high spatial resolution in real time and without radioactive contrast agents. Finally, this approach is highly synergistic with US imaging, which enables multiparametric analysis of each lymph node.

Despite the promising initial results, further studies are needed before clinical translation can be pursued. First, the lymph nodes in this mouse model are relatively superficial, as they are located only a few millimeters beneath the surface of the skin. In clinical practice, imaging depths of 3–5 cm will be required. PA imaging at these depths already has been demonstrated, but the wavelength-dependent attenuation of light in tissue will need to be carefully taken into account. Second, the present study focused on a single metastatic mouse model. Thus,

Figure 5

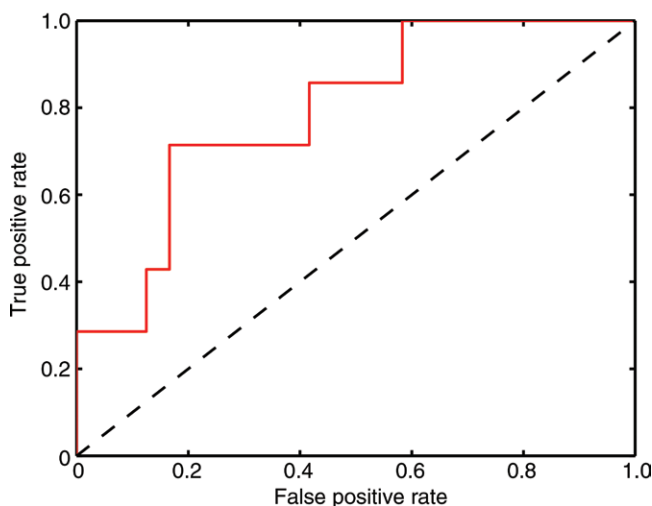


Figure 5: Receiver operator characteristic curve shows SO_2 alone acts as a moderate classifier of micrometastatic lymph nodes. The area under the curve is 0.79.

additional studies that use different models of head and neck, breast, and skin cancer will be initiated to determine the extent to which these functional changes are observed. Third, the sizes of metastases observed in this study were very small. It is not yet clear how sPA images of the lymph

nodes will evolve as the micrometastases continue to grow. This will be addressed in additional studies in which the primary tumor is surgically removed to facilitate longitudinal imaging studies.

In summary, we have shown that sPA imaging is capable of depicting

Tabulated Values for Reported Sensitivity and Specificity

Classification based on SO ₂ Measurements	True Metastatic State of Lymph Node as Determined at Histologic Analysis	
	Metastasis Present	Metastasis Absent
Metastatic	5	9
Not metastatic	2	22

decreased SO₂ that is correlated with the establishment of metastatic foci in lymph nodes of a mouse model of head and neck cancer. These results suggest that sPA imaging has the potential to be a useful tool in the clinical diagnosis and staging of cancer.

Practical application: Once a primary tumor is detected, sPA imaging, when coupled with US imaging, has the potential to provide physicians with comprehensive anatomic and functional information about regional lymph nodes. In fact, if the sensitivity of the combined technologies proves sufficient, many patients could avoid sentinel lymph node biopsy, which is the standard of care for several types of cancer. To that end, we are currently constructing a clinical combined US/sPA imaging system optimized for lymph node imaging in patients with cancer. Because the technique requires no exogenous contrast agents and because it exposes the patient to safe levels of nonionizing radiation, clinical studies can be initiated quickly. Furthermore, the imaging results could be used to help plan radiation therapy, which is less effective when applied to hypoxic tumors (33).

Acknowledgments: We thank Jeffrey Myers, MD, PhD, of the University of Texas MD Anderson Cancer Center for providing the cell line and mouse model, and Konstantin Sokolov, PhD, of the University of Texas MD Anderson Cancer Center for his fruitful discussions.

Disclosures of Conflicts of Interest: G.P.L. disclosed no relevant conflicts of interest. S.Y.E. disclosed no relevant conflicts of interest.

References

- Sleeman J, Steeg PS. Cancer metastasis as a therapeutic target. *Eur J Cancer* 2010;46(7):1177–1180.
- Veronesi U, Paganelli G, Galimberti V, et al. Sentinel-node biopsy to avoid axillary dissection in breast cancer with clinically negative lymph-nodes. *Lancet* 1997;349(9069):1864–1867.
- Gershenwald JE, Thompson W, Mansfield PF, et al. Multi-institutional melanoma lymphatic mapping experience: the prognostic value of sentinel lymph node status in 612 stage I or II melanoma patients. *J Clin Oncol* 1999;17(3):976–983.
- Stoeckli SJ, Steinert H, Pfaltz M, Schmid S. Sentinel lymph node evaluation in squamous cell carcinoma of the head and neck. *Otolaryngol Head Neck Surg* 2001;125(3):221–226.
- Goldberg JI, Riedel ER, Morrow M, Van Zee KJ. Morbidity of sentinel node biopsy: relationship between number of excised lymph nodes and patient perceptions of lymphedema. *Ann Surg Oncol* 2011;18(10):2866–2872.
- Langer I, Guller U, Berclaz G, et al. Morbidity of sentinel lymph node biopsy (SLN) alone versus SLN and completion axillary lymph node dissection after breast cancer surgery: a prospective Swiss multicenter study on 659 patients. *Ann Surg* 2007;245(3):452–461.
- Cohen SM, Fishinghawk BG, Cohen MS. Translational imaging of lymphatics in cancer. *Adv Drug Deliv Rev* 2011;63(10-11):956–962.
- Wunderbaldinger P. Problems and prospects of modern lymph node imaging. *Eur J Radiol* 2006;58(3):325–337.
- Wagner JD, Schauwecker DS, Davidson D, Wenck S, Jung SH, Hutchins G. FDG-PET sensitivity for melanoma lymph node metastases is dependent on tumor volume. *J Surg Oncol* 2001;77(4):237–242.
- Kim S, Lim YT, Soltesz EG, et al. Near-infrared fluorescent type II quantum dots for sentinel lymph node mapping. *Nat Biotechnol* 2004;22(1):93–97.
- Savariar EN, Felsen CN, Nashi N, et al. Real-time in vivo molecular detection of primary tumors and metastases with ratio-metric activatable cell-penetrating peptides. *Cancer Res* 2013;73(2):855–864.
- Ntziachristos V, Ripoll J, Wang LV, Weissleder R. Looking and listening to light: the evolution of whole-body photonic imaging. *Nat Biotechnol* 2005;23(3):313–320.
- Richards PS, Peacock TE. The role of ultrasound in the detection of cervical lymph node metastases in clinically N0 squamous cell carcinoma of the head and neck. *Cancer Imaging* 2007;7(1):167–178.
- Yang WT, Ahuja A, Tang A, Suen M, King W, Metreweli C. High resolution sonographic detection of axillary lymph node metastases in breast cancer. *J Ultrasound Med* 1996;15(3):241–246.
- Yang W, Dempsey PJ. Diagnostic breast ultrasound: current status and future directions. *Radiol Clin North Am* 2007;45(5):845–861, vii.
- Luke GP, Yeager D, Emelianov SY. Biomedical applications of photoacoustic imaging with exogenous contrast agents. *Ann Biomed Eng* 2012;40(2):422–437.
- Mallidi S, Luke GP, Emelianov S. Photoacoustic imaging in cancer detection, diagnosis, and treatment guidance. *Trends Biotechnol* 2011;29(5):213–221.
- Beard P. Biomedical photoacoustic imaging. *Interface Focus* 2011;1(4):602–631.
- Wang LV, Hu S. Photoacoustic tomography: in vivo imaging from organelles to organs. *Science* 2012;335(6075):1458–1462.
- Luke GP, Bashyam A, Homan KA, Makhija S, Chen YS, Emelianov SY. Silica-coated gold nanoplates as stable photoacoustic contrast agents for sentinel lymph node imaging. *Nanotechnology* 2013;24(45):455101.
- Cai X, Li W, Kim CH, Yuan Y, Wang LV, Xia Y. In vivo quantitative evaluation of the transport kinetics of gold nanocages in a lymphatic system by noninvasive photoacoustic tomography. *ACS Nano* 2011;5(12):9658–9667.
- Erpelding TN, Garcia-Urbe A, Krumholz A, et al. A dual-modality photoacoustic and ultrasound imaging system for noninvasive sentinel lymph node detection: preliminary clinical results. In: Oraevsky AA, Wang LV, eds. *Proceedings of SPIE: medical imaging 2014—photons plus ultrasound: imaging and sensing 2014*. Vol 8943. Bellingham, Wash: International Society for Optics and Photonics, 2014; 894359. doi:10.1117/12.2040475.
- Luke GP, Emelianov SY. Optimization of in vivo spectroscopic photoacoustic imaging by smart optical wavelength selection. *Opt Lett* 2014;39(7):2214–2217.
- Luke GP, Myers J, Emelianov S, Sokolov K. Sentinel lymph node biopsy revisited: ultrasound-guided photoacoustic detection of micrometastases using molecularly targeted plasmonic nanosensors. *Cancer Res* 2014;74(19):5397–5408.

25. Zhang HF, Maslov K, Stoica G, Wang LV. Functional photoacoustic microscopy for high-resolution and noninvasive in vivo imaging. *Nat Biotechnol* 2006;24(7):848–851.
26. Myers JN, Holsinger FC, Jasser SA, Bekele BN, Fidler IJ. An orthotopic nude mouse model of oral tongue squamous cell carcinoma. *Clin Cancer Res* 2002;8(1):293–298.
27. Kim S, Chen YS, Luke GP, Emelianov SY. In vivo three-dimensional spectroscopic photoacoustic imaging for monitoring nanoparticle delivery. *Biomed Opt Express* 2011;2(9):2540–2550.
28. Jacques SL. Optical properties of biological tissues: a review. *Phys Med Biol* 2013;58(11):R37–R61.
29. Højsgaard S, Halekoh U, Yan J. The R package geepack for generalized estimating equations. *J Stat Softw* 2006;15(2):1–11.
30. Harris AL. Hypoxia: a key regulatory factor in tumour growth. *Nat Rev Cancer* 2002;2(1):38–47.
31. Van den Eynden GG, Van der Auwera I, Van Laere SJ, et al. Angiogenesis and hypoxia in lymph node metastases is predicted by the angiogenesis and hypoxia in the primary tumour in patients with breast cancer. *Br J Cancer* 2005;93(10):1128–1136.
32. Harisinghani MG, Barentsz J, Hahn PF, et al. Noninvasive detection of clinically occult lymph-node metastases in prostate cancer. *N Engl J Med* 2003;348(25):2491–2499.
33. Zips D, Zöphel K, Abolmaali N, et al. Exploratory prospective trial of hypoxia-specific PET imaging during radiochemotherapy in patients with locally advanced head-and-neck cancer. *Radiother Oncol* 2012;105(1):21–28.